University of Reading

Numerical simulation of the 12 May 1997 CME Event: The role of magnetic reconnection

Article

Published Version

Cohen, O., Attrill, G. D. R., Schwadron, N. A., Crooker, N. U., Owens, M. J. ORCID: https://orcid.org/0000-0003-2061-2453, Downs, C. and Gombosi, T. I. (2010) Numerical simulation of the 12 May 1997 CME Event: The role of magnetic reconnection. Journal of Geophysical Research, 115 (A10). A10104. ISSN 0148-0227 doi: 10.1029/2010JA015464
Available at https://centaur.reading.ac.uk/7972/

It is advisable to refer to the publisher's version if you intend to cite from the work. See Guidance on citing.
Published version at: http://dx.doi.org/10.1029/2010JA015464
To link to this article DOI: http://dx.doi.org/10.1029/2010JA015464

Publisher: American Geophysical Union

All outputs in CentAUR are protected by Intellectual Property Rights law, including copyright law. Copyright and IPR is retained by the creators or other copyright holders. Terms and conditions for use of this material are defined in the End User Agreement.

www.reading.ac.uk/centaur

University of Reading

CentAUR

Central Archive at the University of Reading

Reading's research outputs online

Numerical simulation of the 12 May 1997 CME Event: The role of magnetic reconnection

O. Cohen,[1] G. D. R. Attrill,[1] N. A. Schwadron,[2] N. U. Crooker,[2] M. J. Owens,[3] C. Downs,[4] and T. I. Gombosi[5]

Received 15 March 2010; revised 7 June 2010; accepted 24 June 2010; published 7 October 2010.

[1] We perform a numerical study of the evolution of a Coronal Mass Ejection (CME) and its interaction with the coronal magnetic field based on the 12 May 1997, CME event using a global MagnetoHydroDynamic (MHD) model for the solar corona. The ambient solar wind steady-state solution is driven by photospheric magnetic field data, while the solar eruption is obtained by superimposing an unstable flux rope onto the steady-state solution. During the initial stage of CME expansion, the core flux rope reconnects with the neighboring field, which facilitates lateral expansion of the CME footprint in the low corona. The flux rope field also reconnects with the oppositely orientated overlying magnetic field in the manner of the breakout model. During this stage of the eruption, the simulated CME rotates counter-clockwise to achieve an orientation that is in agreement with the interplanetary flux rope observed at 1 AU. A significant component of the CME that expands into interplanetary space comprises one of the side lobes created mainly as a result of reconnection with the overlying field. Within 3 hours, reconnection effectively modifies the CME connectivity from the initial condition where both footpoints are rooted in the active region to a situation where one footpoint is displaced into the quiet Sun, at a significant distance ($\approx 1R_{\odot}$) from the original source region. The expansion and rotation due to interaction with the overlying magnetic field stops when the CME reaches the outer edge of the helmet streamer belt, where the field is organized on a global scale. The simulation thus offers a new view of the role reconnection plays in rotating a CME flux rope and transporting its footpoints while preserving its core structure.

Citation: Cohen, O., G. D. R. Attrill, N. A. Schwadron, N. U. Crooker, M. J. Owens, C. Downs, and T. I. Gombosi (2010), Numerical simulation of the 12 May 1997 CME Event: The role of magnetic reconnection, *J. Geophys. Res.*, *115*, A10104, doi:10.1029/2010JA015464.

1. Introduction

[2] In recent decades, the concept of magnetic reconnection, in which two oppositely orientated magnetic field lines are cut and re-assembled, has become more accepted as an important process in solar coronal dynamics. In particular, magnetic reconnection seems to dominate the initiation, evolution, and propagation of Coronal Mass Ejections (CMEs), as the magnetic flux carried by the CME interacts with the pre-existing field both in the low corona and throughout the heliosphere. In recent years, a number of CME initiation models have attempted to resolve the observed features of a solar eruption. Many CME initiation models drive the eruption by imposing photospheric shear motion, flux diffusion, and flux cancellation to the footpoints of the pre-existing magnetic field [e.g., see *Forbes and Priest*, 1995; *Amari et al.*, 2000; *Linker et al.*, 2003] and the review by *Forbes et al.* [2006, and references therein]. In other words, the eruption is obtained through modification of the boundary conditions, transforming the initial potential magnetic field into a non-potential, twisted magnetic field, which has the required free energy stored in it. This non-potential state introduces currents so that the Lorentz force overcomes the downward magnetic tension and gravity; eventually, the CME erupts when the force balance breaks down. In this class of CME initiation model, which we refer to as the "driven" model, magnetic reconnection occurs below the CME flux rope in the vicinity of the magnetic field footpoints.

[3] Another type of CME initiation model is the breakout model [*Antiochos et al.*, 1999; *Lynch et al.*, 2008], in which a bipolar region (representing the source active region of the CME) is embedded in a background dipole field of opposite polarity. The eruption in this case is driven by shearing the

[1]Harvard-Smithsonian Center for Astrophysics, Cambridge, Massachusetts, USA.
[2]Center for Space Physics, Boston University, Boston, Massachusetts, USA.
[3]Space Environment Physics Group, Department of Meteorology, University of Reading, Reading, UK.
[4]Institute for Astronomy, University of Hawaii at Manoa, Honolulu, Hawaii, USA.
[5]Center for Space Environment Modeling, University of Michigan, Ann Arbor, Michigan, USA.

Copyright 2010 by the American Geophysical Union.
0148-0227/10/2010JA015464

footpoints of the local bipolar region around its neutral line. As a result, the local bipolar field inflates and begins to reconnect with the oppositely orientated overlying field. This reconnection transfers overlying field to the side lobes, until the CME erupts through the weakened overlying field. The location of magnetic reconnection that drives this type of CME initiation model occurs above the CME flux rope, and there is no opening or disconnection of flux during the process. There are two main problems with most of the current CME initiation models. First, these models use idealized magnetic configurations, which only mimic the realistic coronal field, along with idealized footpoint motions. Second, almost all models neglect the non-potential, background solar wind solution into which the CME is erupting [*Manchester et al.*, 2004; *Lugaz et al.*, 2007; *Cohen et al.*, 2008a]. Taking into account a more realistic coronal environment might significantly affect the propagation of the CME due to the interaction with the more complex ambient field. This three-dimensional interaction can facilitate the lateral expansion of the outer shell of the CME via magnetic reconnection during the eruption [e.g., *Manoharan et al.*, 1996; *Pick et al.*, 1998; *Pohjolainen et al.*, 2001].

[4] One of the observed signatures associated with CMEs in the low corona are the so-called coronal "waves". Since their discovery in 1996 [*Dere et al.*, 1997; *Moses et al.*, 1997; *Thompson et al.*, 1998], the physical nature of EIT coronal waves, which are strongly linked to CMEs [*Biesecker et al.*, 2002] has been under debate. In particular, there is an argument whether the observed coronal "wave" is a MagnetoHydroDynamic (MHD) wave, or whether it corresponds to the actual footprint of the CME (for a complete discussion on this debate see *Cohen et al.* [2009], as well as *Ofman and Thompson* [2002], *Ofman* [2007], and *Schmidt and Ofman* [2010, and references therein]). In one non-wave model, the latter requires the flux rope to reconnect with the surrounding coronal field, facilitating the lateral expansion [*Attrill et al.*, 2007]. This paper demonstrates that the concept can occur in conjunction with the breakout model where the original flux rope reconnects with the overlying field. The main difference between the two is essentially the location of the reconnection point. In the breakout model, the polarity of the CME flux rope is opposite to that of the large-scale overlying field, so that the reconnection occurs at the top of the flux rope. In the model by *Attrill et al.* [2007], which we can call the "stepping reconnection model", reconnection occurs whenever the core flux rope meets a neighboring loop with opposite polarity and the reconnection point is located to the side of the expanding core flux rope. We demonstrate that the stepping reconnection model can theoretically occur within the central part of the breakout model topology, facilitating the expansion of the core flux rope, prior to interaction with the larger-scale overlying field. This concept is discussed in section 4.

[5] In a three-dimensional MHD simulation of a recent CME event (13 February 2009), *Cohen et al.* [2009] have shown that the core flux rope indeed reconnects with the surrounding field in the same manner as described by *Attrill et al.* [2007]. They also showed that the bright front constituting the diffuse EIT coronal waves is composed of both a piston-driven MHD wave as well as non-wave components, which are coupled as long as the CME continues to expand laterally. The lateral expansion essentially stops when the field topology no longer allows the magnetic field to reconnect, and the magnetic overpressure of the flux rope relative to the surroundings no longer drives a strong lateral expansion. From this point, which can be at the considerable distance of $\approx 1R_{\odot}$ from the source region [*Attrill et al.*, 2009; *Cohen et al.*, 2009], only the MHD wave component continues to exist as a freely propagating wave.

[6] The May 1997 CME event is a SHINE campaign event and it has been chosen due to the fact that it was an isolated halo CME event occurred during solar minimum, which supposedly makes it a "simple" event, and due to the relatively extensive observational data of the event. Several attempts to simulate the global evolution of a CME event in the corona and in the heliosphere have been done in the past decade. For example, *Manchester et al.* [2004], *Fan and Gibson* [2007], *Riley et al.* [2008], and *van der Holst et al.* [2009, and references therein] have simulated CME eruptions driven by different methods into either a background corona in hydrostatic equilibrium or a more physical solar wind background. However, even the steady state solar wind solution in these simulations was based on an idealized dipole configuration for the solar magnetic field. The particular May 1997 event has been simulated by *Odstrcil et al.* [2004, 2005], *Shen et al.* [2007], and *Wu et al.* [2007]. All these simulations however, were focused on the propagation of the CME to the Earth, and they were driven by kinematic propagation of the MHD parameters to the inner boundary of the simulation domain, which has been set to be beyond the Alfvénic point.

[7] In this work, we use a model for the solar corona which is driven by high-resolution magnetogram data and provides a more realistic coronal magnetic field. The model also simulates a CME that propagates through a steady-state, non-potential MHD solution for the solar corona and the solar wind. The advantage of such a model is that it enables us to study the complex interaction of the CME with the realistic ambient field. The main limitation of the model is that the CME is a fully-formed flux rope that is "injected" into the steady-state solution with its observed parameters. While reconnection between the closed loops of the flux rope and the surrounding magnetic field is a primary focus of this paper, any reconnection between closed loops beneath the CME that generates flux rope coils, as occurs in many CME initiation models, is not part of our simulation. Another difference between this model and the CME initiation models described previously is that here we are interested in the interaction above the surface with fixed photospheric boundary conditions, while in the other models, modification of the boundary conditions is the main driver for the simulation. We present a high-resolution numerical simulation of the complex interaction between the erupting CME and the ambient coronal field (up to $24R_{\odot}$) based on the 12 May 1997, CME event. The goal of this work is to better understand the three-dimensional interaction of the CME with the ambient flux.

[8] The structure of this paper is as follows. We describe the numerical simulation in section 2 and present the results in section 3. We discuss the consequences and implications

of the simulation results in Section 4 and conclude our findings in section 5.

2. Numerical Model

2.1. Ambient Solar Wind and CME Initiation

[9] For our study, we use the Solar Corona (SC) module [*Cohen et al.*, 2007] of the Space Weather Modeling Framework (SWMF) [*Tóth et al.*, 2005], which is based on the BATS-R-US global MHD code [*Powell et al.*, 1999]. The steady-state solar wind solution is obtained in a non-polytropic manner [*Roussev et al.*, 2003b; *Cohen et al.*, 2007, 2008b] and it is constrained by the empirical Wang-Sheeley-Arge (WSA) model [*Wang and Sheeley*, 1990; *Arge and Pizzo*, 2000]. We use a potential magnetic field [*Altschuler and Newkirk*, 1969] to prescribe the initial condition for the magnetic field using high-resolution MDI magnetograms (available at http://sun.stanford.edu/synop/), and the steady-state is obtained by iterating the MHD equations:

$$\begin{gathered}\frac{\partial\rho}{\partial t}+\nabla\cdot(\rho\mathbf{u})=0,\\ \rho\frac{\partial\mathbf{u}}{\partial t}+\nabla\cdot\left(\rho\mathbf{u}\mathbf{u}+pI+\frac{B^2}{2\mu_0}I-\frac{\mathbf{B}\mathbf{B}}{\mu_0}\right)=\rho\mathbf{g},\\ \frac{\partial\mathbf{B}}{\partial t}+\nabla\cdot(\mathbf{u}\mathbf{B}-\mathbf{B}\mathbf{u})=0,\\ \frac{\partial}{\partial t}\left(\frac{1}{2}\rho u^2+\frac{1}{\gamma-1}p+\frac{B^2}{2\mu_0}\right)+\\ \nabla\cdot\left(\frac{1}{2}\rho u^2\mathbf{u}+\frac{\gamma}{\gamma-1}p\mathbf{u}+\frac{(\mathbf{B}\cdot\mathbf{B})\mathbf{u}-\mathbf{B}(\mathbf{B}\cdot\mathbf{u})}{\mu_0}\right)=\rho(\mathbf{g}\cdot\mathbf{u}),\end{gathered}\tag{1}$$

where ρ, $\mathbf{u}$, $\mathbf{B}$, p, $\mathbf{g}$, and γ are the mass density, velocity, magnetic field, pressure, gravity, and the polytropic index, respectively, until convergence is achieved.

[10] We initiate the CME by superimposing an unstable, semi-circular flux rope based on the analytical model by *Titov and Démoulin* [1999] on top of the ambient solution [*Roussev et al.*, 2003a]. The flux rope properties are matched to fit the observed properties of the source active region and its inversion line. The free energy is controlled by an additional toroidal field that produces the observed linear speed of the CME. The simulation here is based on a previous simulation done by *Cohen et al.* [2008a], which includes full propagation of the CME to 1 AU and comparison with in-situ data. The CME initiation method described here has been used to study processes in the solar corona [e.g., *Lugaz et al.*, 2007; *Manchester et al.*, 2008].

2.2. Simulation Setup

[11] In order to follow the topology and evolution of the magnetic interaction between the CME and the ambient field, we design the grid with high resolution around the active region and along the line of CME propagation. The grid size around the active region is 10^{-3} $R_\odot$, and the grid size along the propagation line is 10^{-2} $R_\odot$. The grid resolution is coarser in other regions of the simulation domain, which are not of interest in the context of this work. The time step in the simulation is determined by the Alfvén speed and the grid resolution. The higher the magnetic field and smaller the grid size, the smaller the time step. In order to compensate for the extremely small time steps in active regions, where magnetic fields are very strong, we set the inner boundary of the simulation to be at a height of $0.06R_\odot$ above the surface, where the magnetic field is weaker.

[12] Figure 1 displays the initial stage of the simulation. Figure 1 (left) shows the large-scale structure of the steady-state corona, with selected closed field lines in blue and open field lines in red. The background color contours represent the solar wind radial speed, ranging from fast in yellow to slow in blue. Figure 1 (right) shows the vicinity of the active region at the initial state of the simulation, where its approximated location on the Sun is marked by the black square. Color contours represent the magnitude of the radial field on a sphere at a height of $1.06R_\odot$, red streamlines represent three-dimensional magnetic field lines of the superimposed flux rope, and solid white lines mark the grid structure around the flux rope. The flux rope itself is represented by an iso surface of mass density, $\rho = 10^{-14}$ g cm^{-3}, which is greater than the surrounding density at the same height.

2.3. Concept of Numerical Reconnection in the Global Model for the Solar Corona

[13] The model solves the set of ideal MHD equations, so no physical resistivity is introduced in the equations. Therefore, the rate of *numerical* magnetic reconnection in the simulation is, in principle, controlled by numerical diffusion term, which is designed to stabilize the numerical solution and is not directly related to the physical resistivity of the system. The value of the numerical diffusion is proportional to the size of the grid cell and the time step via the ratio $\Delta x^2/\Delta t$. In the case of the numerical resistivity in the induction equation (where it can affect magnetic reconnections) this ratio is proportional to η/μ_0, where μ_0 is the permeability of free space, and η is the electric resistivity. In the solar corona, the typical value for the Lundquist number, $S = \mu_0 L v_A/\eta$ is 10^{12}–10^{14} [*Boyd and Sanderson*, 2003], where L is the typical length scale, and v_A is the Alfvén speed. The typical value of Δx is a fraction of a solar radius and the time step can range between 0.1–10 s. Therefore, using the same typical values for L and v_A as above, we find that $1 < S_n = L v_A \Delta t/\Delta^2 x \ll S$, where S_n is the Lundquist number calculated using the numerical resistivity. This means that the model might result in over-reconnection of the magnetic field in regions where two opposite magnetic field lines are pushed towards each other. An example for such numerical behavior is the generation of "U-shape" detached field lines around the heliospheric current sheet. This issue is resolved by implementing the Roe solver in the numerical model, which is a more precise, less diffusive numerical scheme, and is equivalent to the addition of one more level of grid refinement (regardless of the actual smallest grid size). The Roe solver and its implementation to the MHD model are discussed in detail by *Sokolov et al.* [2008].

[14] When discussing the magnetic reconnection of a CME with the coronal ambient field, one should keep in mind that this reconnection has a global, macroscopic sense, and that the time scale for such reconnection (which can be

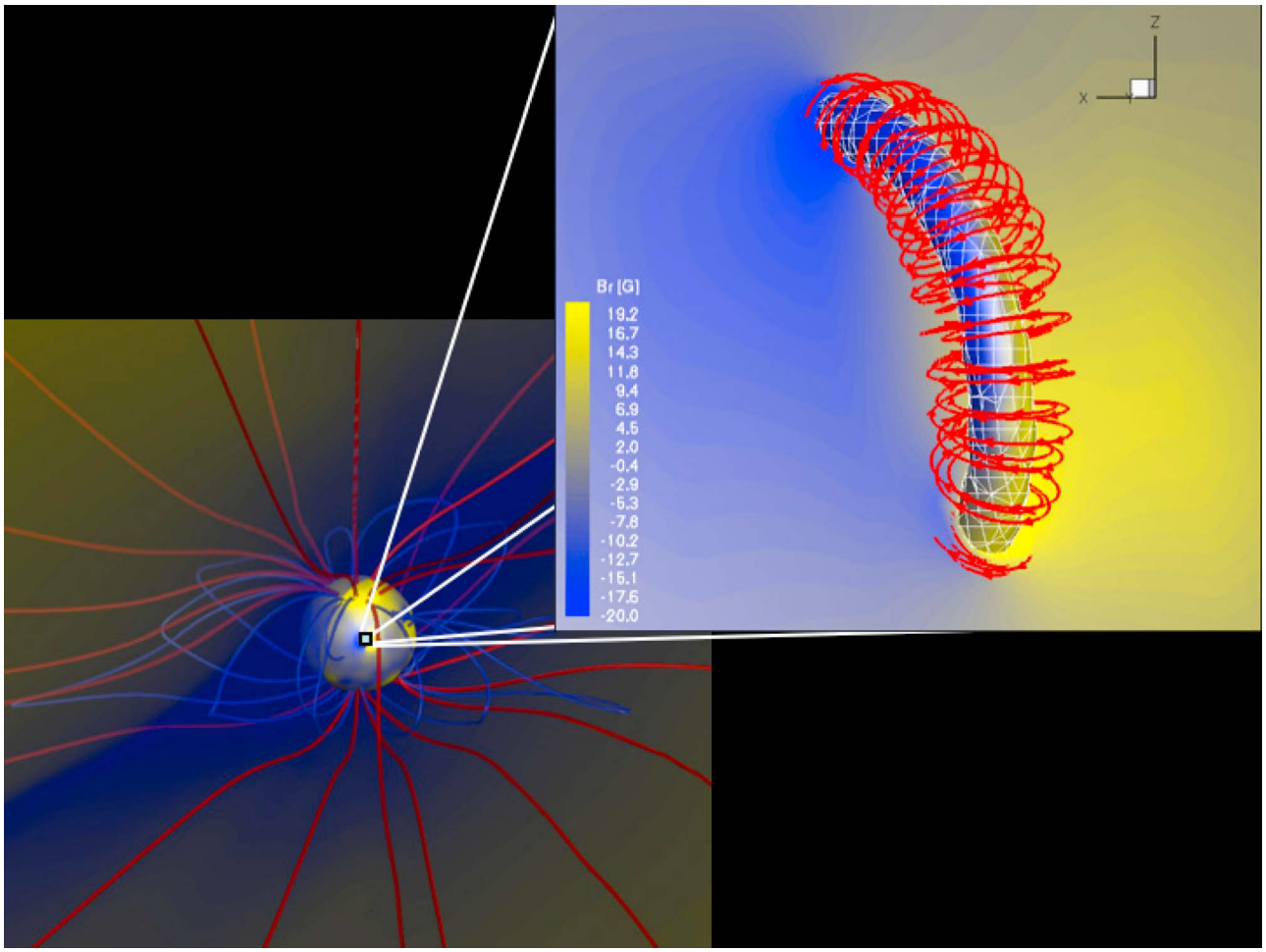

Figure 1. (left) The large-scale structure of the steady-state corona. Selected field lines are shown: closed field lines (blue) and open field lines (red). Background color contours represent the solar wind radial speed (yellow, fast; blue, slow). (right) The vicinity of the active region at the initial state of the simulation, where its approximated location on the Sun is marked by the black square. Color contours represent the magnitude of the radial field on a sphere at a height of $1.06R_{\odot}$, red streamlines represent three-dimensional magnetic field lines of the superimposed flux rope, and solid white lines mark the grid structure around the flux rope. The flux rope itself is represented by an iso surface of mass density, $\rho = 2 \cdot 10^{-14}$ g cm^{-3}, which is greater than the surrounding density at the same height.

of the same order as the Alfvénic time scale) depends on the CME size and speed. In the simulation presented here, we try to capture this global interaction between the newly injected magnetic flux carried by the CME and the pre-existing field. This concept is different from the microscopic description of magnetic reconnection that obviously needs a better treatment than a global MHD model. In this simulation, we focus our study on the re-distribution of the global field as the new flux is introduced into the system, and on how the interaction between the fields affects the propagation of the CME through the corona. We compare our results with observations of large-scale signatures for such interaction between the fields in the corona. We emphasis that any further mentioning in the text for the term "magnetic reconnection" refers to a numerical reconnection in the simulation.

[15] We simulated the first 20 hours of propagation using the PLEIADES cluster at NASA's NAS center. The CME front left the simulation domain after approximately 14 hours.

3. Results

[16] We separate the analysis of the results into two parts. First, we validate the timing and the overall structure of the CME with some observations, and, second, we analyze the results assuming the overall interaction is satisfactorily captured by the simulation. Figure 2 compares the observed and simulated coronal dimmings and the observed and simulated coronal wave front associated with the density changes due to the CME expansion and propagation through the corona [after *Cohen et al.*, 2009]. The rows display comparisons for the early stages of the simulation, 10, 30, 40, and 60 minutes after the eruption onset, from top to bottom. Figure 2a shows SOHO EIT 195*Å* base-difference images, constructed with data from http://sohowww.nascom.nasa.gov. Figure 2b

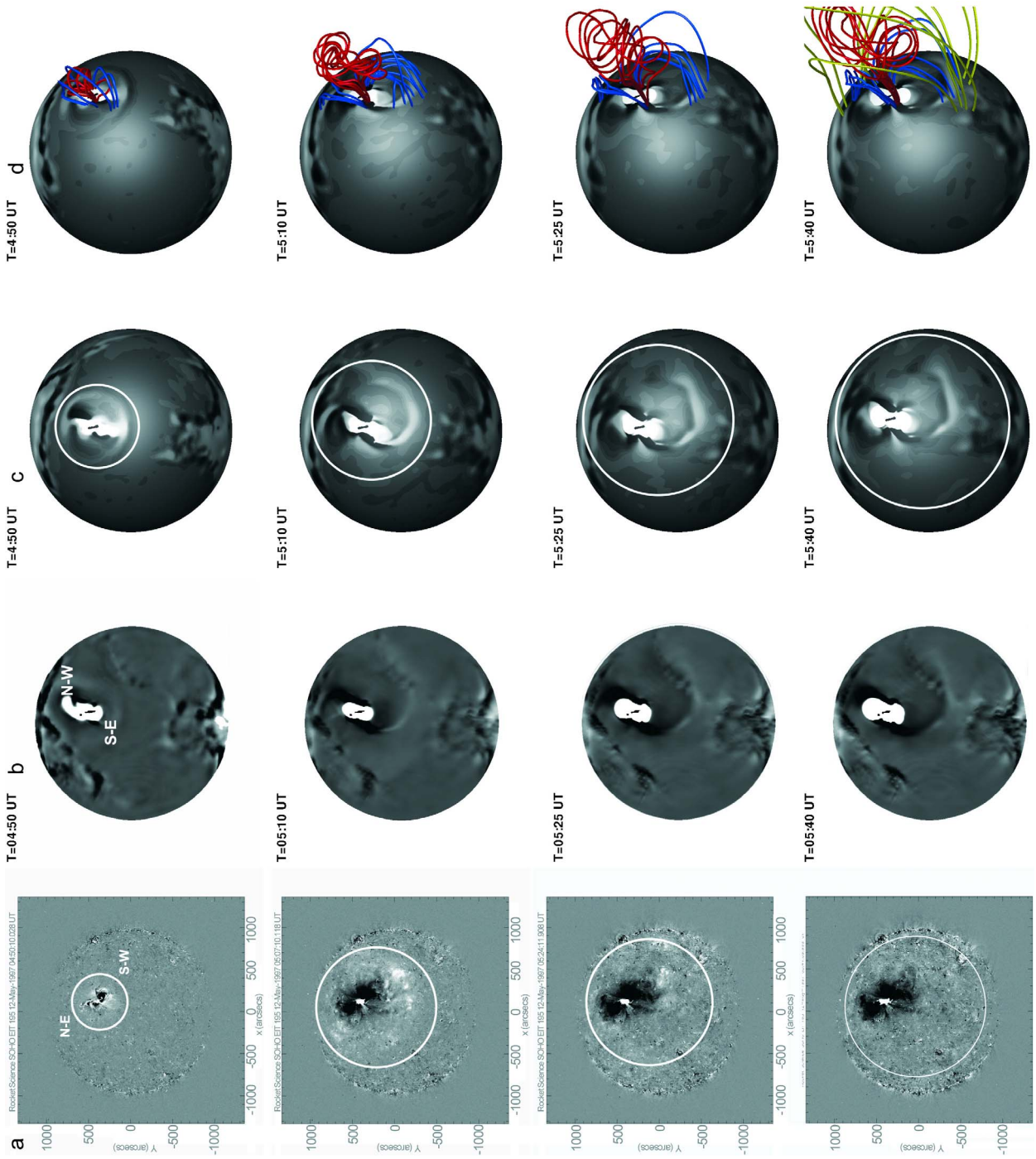
a
b
c
d
T=04:50 UT
T=05:10 UT
T=05:25 UT
T=05:40 UT
T=4:50 UT
T=5:10 UT
T=5:25 UT
T=5:40 UT
N-E
S-W
N-W
S-E
Y (arcsecs)
x (arcsecs)

Figure 2

shows the corresponding synthetic EIT 195Å base-difference images produced by the simulation. These images are the line of sight integral: $\int n_e^2 R(n_e, T)dl$, where n_e is the electron number density and R is the response function for the EIT 195Å filter based on spectral synthesis from the CHIANTI code [*Landi et al.*, 2002]. The complete description of the synthetic EIT images in SWMF can be found in the work by *Downs et al.* [2010]. Figure 2c shows base-difference images of the simulated mass density on a sphere at height of $r = 1.1R_\odot$. The differences are normalized to the pre-eruption mass density distribution in a similar manner as in the work by *Cohen et al.* [2009]. Figure 2d shows a display that is similar to Figure 2c but with the addition of selected magnetic field lines. Those in the core flux rope are marked in red, those with one footpoint rooted in the original source region are marked in blue, and overlying field lines with both footpoints located far from the source region are marked in yellow. The approximate location of the leading edge of the coronal wave disturbance is marked by a white circle in Figures 2a and 2c.

[17] Figure 2 shows that the strongest brightening in the synthetic EIT images (Figure 2b) lags behind the matching observed (Figure 2a) and simulated (Figure 2c) coronal wave fronts, and it remains there in a location comparable to the location of persistent brightenings observed in the base difference images in Figure 2a [see *Attrill et al.*, 2007; *Delannée*, 2009]. Although the locations of the observed and simulated wave fronts match, the latter appears only as a weak density enhancement. On the other hand, the source region of the event appears bright both in the synthetic EIT images and in the density difference images. A discrepancy between the observed and simulated patterns is the lack of any rotation of the coronal wave in the simulation. *Podladchikova and Berghmans* [2005] and *Attrill et al.* [2007] independently showed that in the EIT observations the coronal wave undergoes an overall counter-clockwise rotation. Another discrepancy concerns the coronal dimmings. The NW-SE orientation of the main pair of dimmings in the simulated images appears as the mirror reflection of those in the observations (NE-SW). Coronal dimmings located on either side of a post-eruption arcade are understood to be the footpoints of the flux rope [e.g., *Webb et al.*, 2000]. A possible reason for these discrepancies is that the flux rope in the simulation is idealized and undergoes only a straightforward expansion. Real flux ropes can be much more complicated, with twist and writhe that might lead to the observed rotation of the coronal wave and a different representation of the dimmings.

[18] The global field topology as shown in Figure 2d is similar to the topology extrapolated using a potential field method [*Delannée*, 2009, Figure 2]. This is not surprising, since the ambient magnetic field lines in the low corona are almost potential, even in the MHD solution. The main differences between the MHD solution and the potential field appear in the field lines that are stretched by the solar wind in the high corona and in the field lines of the superimposed flux rope, which are twisted. Unlike the potential field method, the time-dependent, MHD simulation enables us to follow the temporal evolution of the magnetic field and its dynamic response to the CME expansion.

[19] Figure 3 shows snapshots of the evolution of the field topology from the start of the simulation (Figure 3 (top)) to one (Figure 3 (middle)) and four (Figure 3 (bottom)) hours later. Figure 3 (left) shows the photosphere colored with contours of B_r intensity along with selected magnetic field lines (which are not the same in all frames). Magenta marks field lines in the core CME flux rope, with both footpoints located at the source region. Cyan marks overlying field lines with one footpoint rooted in the source region, and yellow marks field lines of the overlying helmet streamers and open field lines with footpoints located far from the source region. Figure 3 (middle) shows that after one hour, some legs of the three-dimensional CME (represented by the highly twisted field lines in cyan, magenta or yellow) have expanded beyond the original active region so that there are more cyan field lines and fewer magenta ones. After four hours, Figure 3 (bottom) shows that many field lines of the CME are located far from the source active region, though we emphasize that some still remain rooted at the original source AR. While the CME dynamic expansion pushes the surrounding field lines to the sides, the only way the footpoint of the CME can migrate away from the source AR is through reconnection with surrounding field lines as the CME is expanding. By the time the CME reaches the height of the large helmet streamers and the open flux that have opposite polarity to that of the CME, the CME footpoint expansion stops and only the traditional volumetric expansion of the CME continues. The overall field evolution at this point in the simulation is roughly consistent with the idealized scenario suggested by the breakout model, probably due to the similar field topologies of the idealized and real cases.

[20] Figure 3 (right) shows a sphere at height $r = 1.06R_\odot$ colored with the sign of B_r for the initial state of the simulation, where positive is yellow and negative is blue. Overlain on this initial polarity pattern is the time-evolving polarity inversion line in red. Figure 3 (middle) and 3 (bottom) show that the inversion line changes as the CME propagates and interacts with the surrounding field. This change in the distribution of positive-negative flux reflects the exchange of closed flux between the CME and the surrounding field.

[21] In order to validate the simulated CME flux rope as it propagates into interplanetary space, we extract the simulated

Figure 2. Comparison of observed and simulated coronal dimmings and the coronal wave for the early stage of the simulation: (top to bottom) 10, 30, 40, and 60 minutes after the eruption onset. (a) SOHO EIT 195Å base-difference images; (b) the corresponding synthetic EIT 195Å base-difference images produced by the simulation. (c) Base-difference images of the simulated mass density on a sphere at height of $r = 1.1R_\odot$. (d) A similar display to Figure 2c, but with the addition of selected magnetic field lines of the core flux rope marked in red, selected field lines with one footpoint rooted in the original source region in blue, and selected overlying field lines with both footpoints located far from the source region in yellow. The white circle in Figures 2a–2c indicates the approximate location of the leading edge of the coronal wave disturbance.

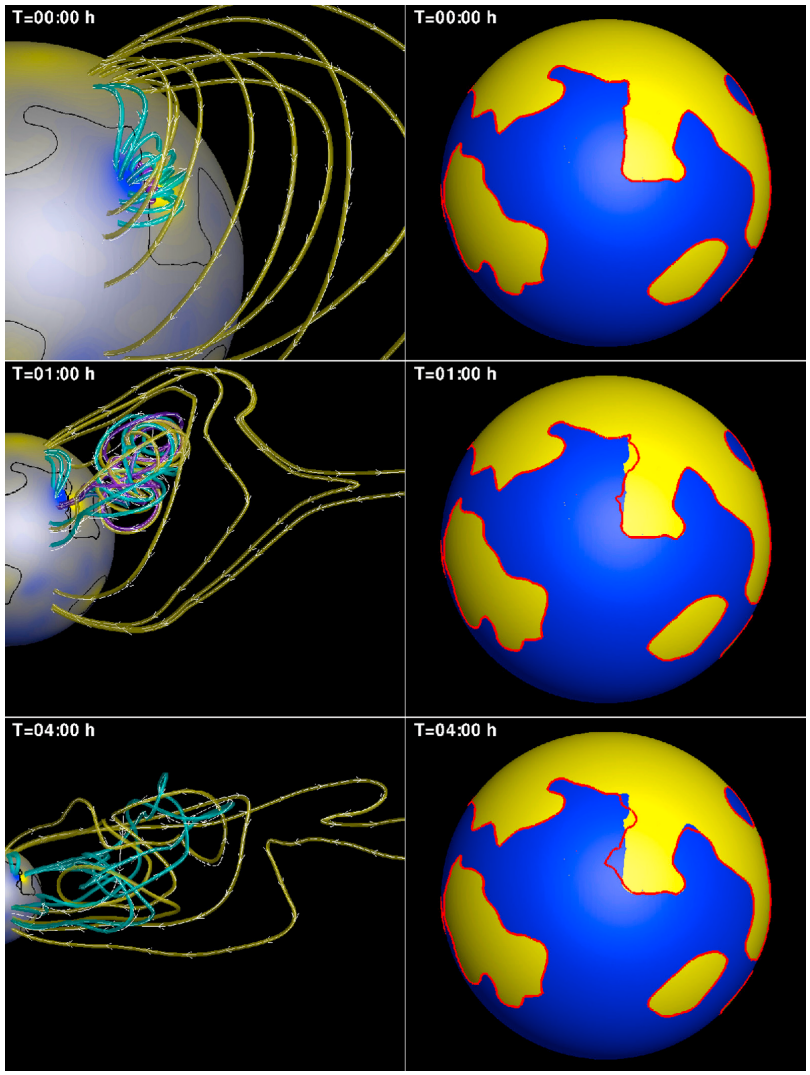

Figure 3. Evolution of the field topology at later time of the simulation than shown in Figure 2. (left) The photosphere colored with contours of B_r intensity, along with selected magnetic field lines. Magenta field lines correspond to the core CME flux rope, with both footpoints rooted in the source region. Cyan lines mark overlying field with one footpoint located at the source region, and yellow lines mark field lines of the overlying helmet streamers and open field lines with footpoints located far from the source region. (right) A sphere at a height of $r = 1.06R_\odot$ colored with the sign of B_r (positive-yellow, negative-blue) for the initial state of the simulation. The red line marks the inversion line for the particular time frame.

plasma parameters across the flux rope (upstream to downstream) from the frame of t = 10h after the eruption onset. We cannot directly compare our simulation result with 1 AU in-situ data, since the simulated CME only reaches ~23–24$R_\odot$, and the coordinate systems of the two data sets are different (Heliocentric Carrington system in the simulation versus Geocentric system for in-situ data). However, we can compare the flux rope orientation and chirality through the local B_z component and assume these should be conserved from the simulated location of the CME to 1 AU.

[22] Figures 4a–4c show a line extraction of B, B_r, and B_z along constant latitude and longitude from upstream (un-shocked plasma) to downstream (shocked plasma) in the simulation frame of reference. Figure 4d shows the GSE B_z component observed by the Wind spacecraft during May 14–16 (data taken from http://cdaweb.gsfc.nasa.gov/). It can be seen that the field rotation, indicated by the change of sign in B_z, is present in the simulation as in the observations (compare Figures 4c and 4d). However, we note that the magnitude of the simulated B_z is greater than in the observations. This may be attributed to the simulation data being extracted closer to the Sun than the 1 AU observations. Here we do not attempt to match the result of the model with this observation, which has been taken at different location in the heliosphere and in different coordinate system, only to demonstrate that the field rotation seen in the data also appears in the simulation.

[23] A visualization of the field topology (also showing the line of extraction) is displayed in Figure 5. Figure 5 (left) shows the photosphere as the inner sphere colored by radial

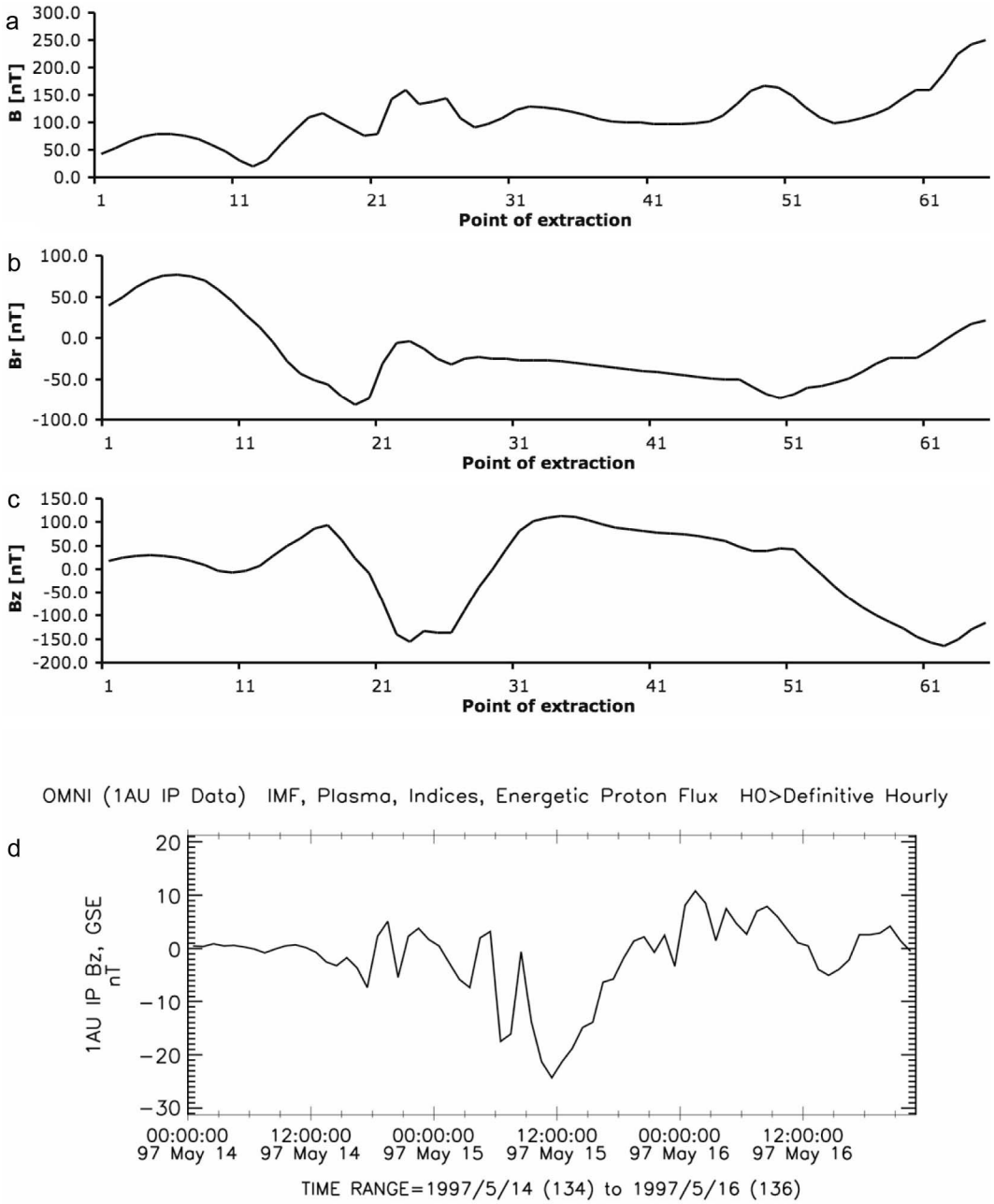

Figure 4. (a–c) Upstream to downstream line extraction of B, B_r, and B_z, respectively, in the simulation frame of reference. (d) The GSE B_z observed by the Wind spacecraft between May 14–16.

field strength. The approximate CME front is shown by the gray shading, which outlines an iso-surface of density ratio equal to 4 between the t = 10h frame and the initial state. Selected field lines illustrate the field topology. Blue and red indicate negative and positive values of B_z, respectively, and the cartoon of a hand indicates the left-handed chirality of the flux rope, where the thumb points in the direction of the axial field and the fingers curl in the direction of the coils. These are in agreement with the line plots of B_z in Figure 4, representing a transition from a downward field (negative B_z) at the front of the CME to an upward field (positive B_z) at the back. The signature is a smooth rotation of the field direction, indicating the passage across the core of a flux rope. This is one of the most distinctive signatures of a magnetic cloud [*Burlaga et al.*, 1981]. The CME topology in Figure 5 (left) is also consistent with the observed interplanetary magnetic cloud shown in the white inset in the lower right corner [from *Crooker et al.*, 2008]. Figure 5 (right) shows a view looking down on the ecliptic plane, which is colored with contours of the solar wind speed. Selected field lines are shown in black, and the blue arrow indicates the line of extraction used for the plots in Figure 4.

[24] Figure 6 shows the orientation of the flux rope at different stages of the simulation, where the display is similar to Figure 5 (left). It can be seen that the rotation is well established about 6 hours after the eruption onset and

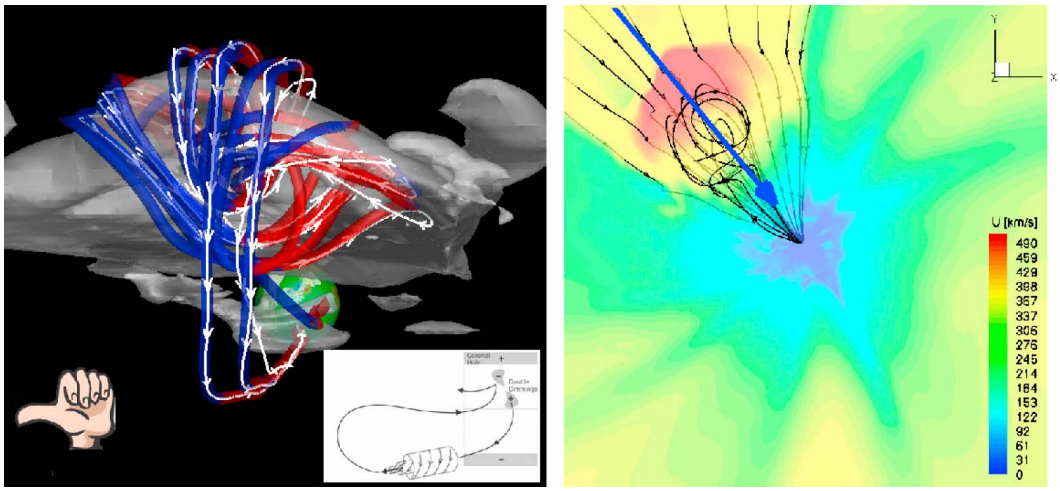

Figure 5. The field topology at t = 10h. (left) The photosphere as the inner sphere colored with the radial field line contours. The approximate CME front is shown by the white shade, which indicates an iso-surface of density ratio of 4 between the t = 10h frame and the initial state. Selected field lines show the front of the CME and the field topology. Blue color indicates negative value of B_z, red color indicates positive value of B_z, and the left-hand cartoon represents the flux rope chirality. Inset shows the observed interplanetary magnetic cloud chirality and orientation [from *Crooker et al.*, 2002]. (right) A view on the equatorial plane colored with contours of the solar wind speed together with selected three-dimensional field lines. The blue arrow marks the upstream-downstream line of extraction shown in Figure 4.

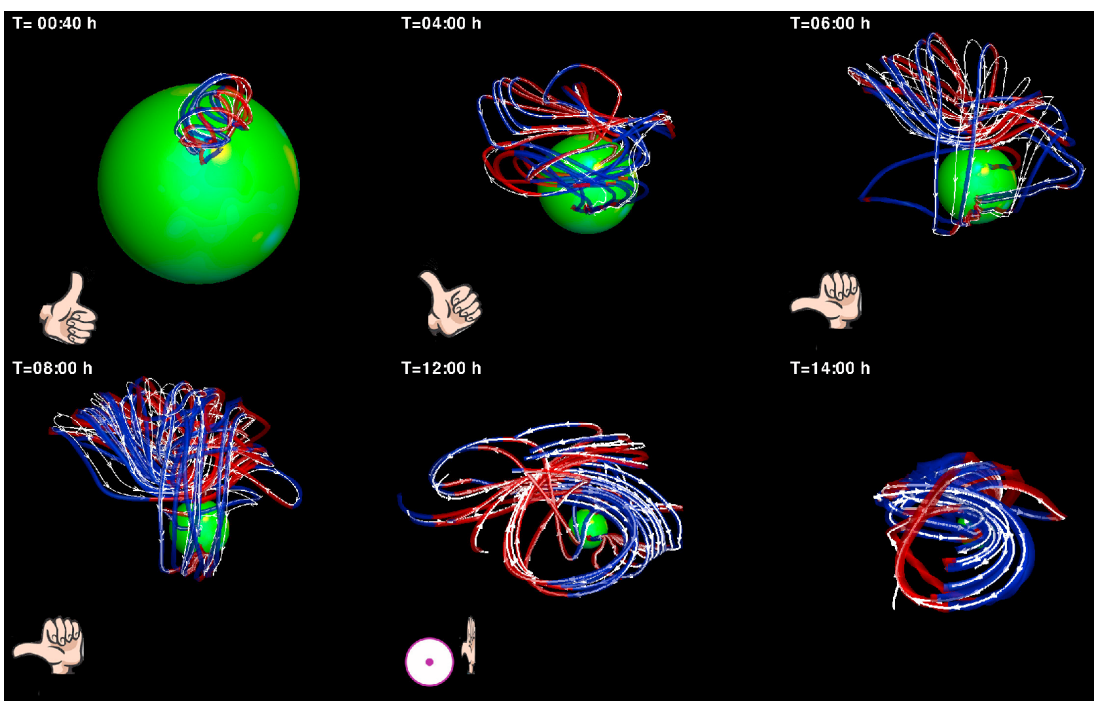

Figure 6. The orientation of the flux rope at different stages of the simulation. Display is similar to Figure 5 (left). Blue (red) indicates negative (positive) B_z. The orientation of the flux rope axis is initially ~N-S (cf. Figure 1). By 00:40 h, the orientation of the axis is NW-SE. In the frame at 04:00 h, the orientation is hard to establish, but by 06:00 h, the axis of the flux rope lies ~E-W. The last two frames at 12:00 h and 14:00 h are taken when most of the CME has left the simulation box.

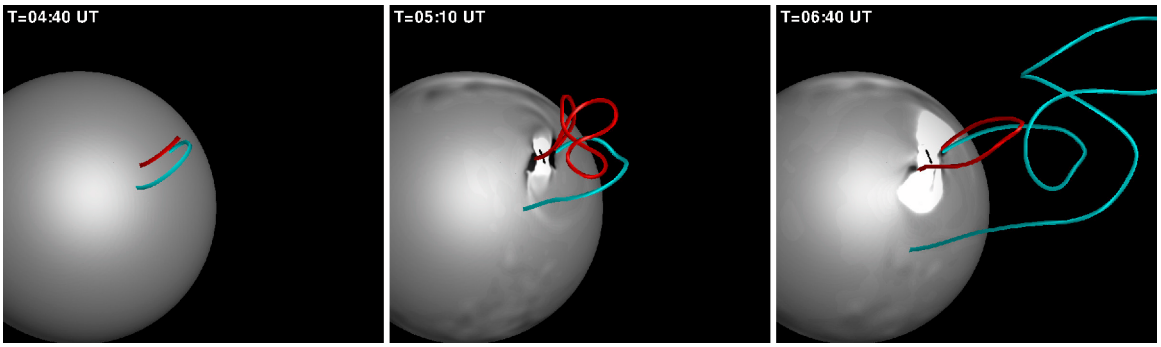

Figure 7. Displacement of the CME footpoints via stepping reconnection with neighboring magnetic field. The figure shows selected field lines and their evolution in time. Density base differences at a height of $r = 1.1R_{\odot}$ are shown in grey (as in Figure 2). (left and middle) The red line indicates the flux rope and has both footpoints rooted in the source AR. The cyan field line has only one footpoint rooted in the source AR, and represents a neighboring field line. In all frames, twisted field lines are associated with the CME. The CME initially expands with its flux rope footpoints (red) located near to the active region (Figure 7 (middle)). (right) Later on, reconnection has occurred between the expanding flux rope (red), and the neighboring field line (cyan). This mechanism migrates the footpoints of the field lines associated with the CME away from the source AR and facilitates a lateral expansion of the CME. The CME footprint thus expands to a large extent in the low corona.

that, after this, the CME maintains its orientation (it can still rotate around the z-axis). This result is also consistent with the overall behavior of the flux rope rotation described by *Lynch et al.* [2009], who used the breakout model in a topologically idealized numerical simulation to study the flux rope rotation. In their model, a rotation of ~40–50 degrees is established during the first ~20 minutes of the flare onset (co-temporal with an increase in the magnitude of the poloidal magnetic field). They ascribe the rotation primarily to the Lorentz force and overall torque from the sheared core magnetic field and related tension forces and conclude that the kink instability [e.g., *Kliem et al.*, 2004] [see also *Green et al.*, 2007] is not responsible. We cannot study the possible effects of the kink instability in our simulation because the Titov-Demoulin flux rope is idealized and no kink-unstable twist is introduced. Our simulation results seem to imply that the flux rope rotation is strongly influenced by interaction with the surrounding field, since the rotation is established at the early stage of the CME propagation, between 04:00 and 06:00 h (Figure 6).

[25] In Figure 7, we display selected field lines and show their evolution in time in order to illustrate the stepping reconnection between the CME and adjacent loops, as described in section 1. Unlike the field lines in Figure 3, here the same field lines are displayed in the different time frames. The sphere represents the photosphere colored with the density base differences as in Figure 2d. In Figure 7 (left) and 7 (middle), the red line indicates the flux rope and has both footpoints rooted in the source AR. The cyan field line represents a neighboring field line with only one footpoint rooted in the source AR. The CME initially expands with its flux rope footpoints (red) located in the active region (Figure 7 (middle)). Later on (Figure 7 (right)), reconnection has occurred between the expanding flux rope (red), and the neighboring field line (cyan). This reconnection transfers part of the original twisted flux rope field to the neighboring loop. The expanded flux rope now has only one footpoint in the source active region. The other has been "stepped out" and is now rooted in the quiet Sun at a considerable distance from the active region. The results displayed in Figure 7 give an example of how one field line in a CME expands laterally as a result of magnetic reconnection between the core flux rope and surrounding magnetic field. This mechanism migrates many of the footpoints of the field lines associated with the CME away from the source AR and thus facilitates a global lateral expansion of the CME in the low corona [*van Driel-Gesztelyi et al.*, 2008].

4. Discussion

[26] The results of our numerical simulation show that in the low corona the CME interacts with the surrounding field, which is composed of magnetic loops with different sizes, orientations, and mixed polarity. The path of CME expansion in this region is determined by the easiest way the CME can get through the surrounding field structure. This path depends on where the magnetic tension is smallest (i.e., in larger overlying loops) and where the field topology allows the CME to reconnect with surrounding field lines. The latter leads to a lateral expansion of the CME via migration of the CME footpoints. In addition, the simulation results show that the left-handed flux rope rotates counterclockwise by 90 degrees by the time the CME has expanded into interplanetary space so that the original ~N-S orientation of the flux rope (see Figure 1), is now aligned ~E-W. This is consistent with the orientation of the magnetic cloud in the ecliptic plane deduced from observations [*Webb et al.*, 2000] and from modeling [*Attrill et al.*, 2006]. Both the CME lateral expansion and rotation wane when the CME starts to interact with the more organized magnetic flux of the large-scale helmet streamers and open flux.

[27] It is reasonable to believe that since both the CME rotation and expansion in our simulation are the result of the interaction between the expanding flux rope and the ambient

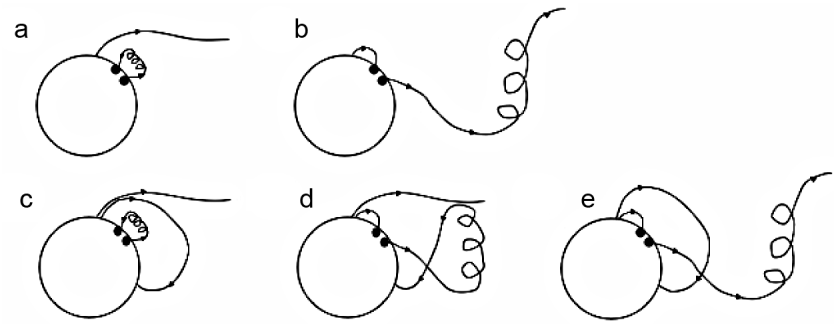

Figure 8. (a and b) The scenario of the event as proposed by *Crooker and Webb* [2006], *Attrill et al.* [2006], and *Crooker et al.* [2008]. The CME is represented by the twisted field line in Figure 8a and it undergoes ICX with an open field line of the north polar coronal hole. (c and d) The scenario based on the simulation results. The core flux rope first reconnects with an overlying closed field line, so closed loops (making up the north side lobe), form between the polar coronal hole and the north dimming region. At the same time, the connectivity of the twisted closed loops that constitute the CME is changed, so that a significant portion of the CME is effectively displaced and expands out into the heliosphere. (e) This extended twisted CME field can later reconnect with an open polar field line.

flux via magnetic reconnection, the sense of the rotation is related to the chirality of the flux rope as well as the orientation of the ambient field, as suggested by *Lynch et al.* [2005]. We further suggest that the final orientation of the flux rope represents the "relaxed" state of the reconnection process between the core flux rope and the surrounding coronal field.

[28] Overall, our simulation produces results that are consistent with the breakout model, primarily because the topology of the ambient field and the core flux rope for the 12 May 1997, event is similar to the idealized field topology in the breakout model. One should keep in mind, however, that this might not be the case during solar maximum, when both the ambient field and the orientation of the core flux rope are unlikely to fulfill such idealized conditions. In addition, we stress that in the breakout model the field topology drives the eruption, while our simulation captures the post-eruption interaction between the CME and the ambient field.

[29] The result of the simulation suggests a scenario which enables us to develop a more complete picture of the 12 May 1997, eruption. Figures 8a and 8b illustrate the scenario proposed earlier by *Crooker and Webb* [2006], *Attrill et al.* [2006], and *Crooker et al.* [2008], as well as *Owens et al.* [2007]. The CME, represented by the twisted line in Figure 8a, expands and eventually undergoes interchange reconnection (ICX) with an open field line of the north polar coronal hole. As a result, the magnetic field in the CME that is rooted in the south dimming region is essentially an open field line (Figure 8b), consistent with the open fields deduced from electron observations in the magnetic cloud at 1 AU. The accumulation of progressively larger closed loops between the northern dimming region and the polar coronal hole has the effect of contracting the northern dimming region, which is well underway by 08:26 UT [see *Attrill et al.*, 2006, Figure 4]. The south dimming region remains near its maximum spatial extent for a longer time than the north dimming region, but by 15:00 UT, it has started to contract, as well. This contraction was not clearly addressed by *Crooker and Webb* [2006] and *Attrill et al.* [2006]. Why should the south dimming region should show a systematic contraction when the field lines rooted in that region should remain open (Figure 8b)?

[30] Our simulation suggests a slightly different scenario, that provides an answer to that question. In this scenario, illustrated in Figures 8c and 8d, the core flux rope first reconnects with greatly extended overlying closed field lines. As a result, the legs of the twisted closed loops that constitute the CME are displaced so that only the south dimming region remains connected to the greatly expanded twisted CME loops (Figure 8d). We note that a flux rope is made up of many complex twisted magnetic field lines. The outermost field lines reconnect with the surrounding magnetic field, but the innermost core field lines may not experience such reconnections. As a result, some part of the original flux rope may remain rooted in the source region throughout the eruption (not shown in Figure 8). Indeed, such a picture is consistent with the deepest parts of coronal dimming regions remaining dimmed for several days [e.g., *Attrill et al.*, 2008], long after the main bulk of a CME has left the Sun.

[31] The contraction of the south dimming region in this 12 May 1997, event can now be explained as a result of successively larger closed loops being formed due to ongoing breakout-type reconnections, so contracting the south dimming in a similar manner to the north one, albeit at a later time due to the much larger scale of these closed loops. During this process, one of the legs of the twisted field making up the CME is displaced out of the source AR. To our knowledge, this is the first time that a CME has been shown to comprise one of the side lobes created as a result of reconnection with the overlying field. Usually the central flux system in the breakout model erupts as the restraining overlying field is removed to the side lobes. Here the situation differs markedly from the textbook breakout scenario in several ways: (1) the reconnection occurs much closer to one footpoint of the overlying closed field than the other, introducing a marked asymmetry; and (2) the overlying closed field is greatly extended so that upon reconnection, relatively long field lines constitute the side lobe and become dragged out into interplanetary space as the eruption pro-

ceeds. These two factors mean that the north dimming region will start to contract, whilst the south region will remain extended for a longer time, as observed.

[32] What the new scenario in Figure 8 may struggle to explain is the unidirectional streaming of suprathermal electrons in the CME at 1 AU, indicating field lines connected to the Sun at only one end. Although the determination of magnetic connectivity from suprathermal electron data can be hindered by significant uncertainties [e.g., *Riley et al.*, 2004], in this case the signature of open fields throughout most of CME is quite clear. In contrast, our simulation results show that the extended twisted field identified as the CME is connected to the Sun at both ends, which topologically would be expected to produce counter-streaming electrons at 1 AU. Two possible explanations for this disagreement are (1) although not apparent in the simulation, the reconnection with overlying loops pictured in Figure 8b may proceed until the supply of closed loops gives way to the neighboring open polar field, in which case the scenario essentially reverts to the original one where interchange reconnection in the corona opens the loops (Figure 8e); (2) interchange reconnection opens the loops associated with the CME, but takes place gradually, in the solar wind, outside the simulation box, in transit to 1 AU.

[33] The first explanation suggests that the helmet streamer (forming the initial overlying closed magnetic field) is temporarily removed by the breakout process, and then later reforms through ICX with the open flux of the polar region. Even though we believe that the ICX scenario represented by Figure 8e must occur at some point, it is hard to capture this interaction in the current simulation (in contrast to the interaction with the closed flux). This may be due to the fact that the ICX interaction should occur closer to the outer boundary, where every field line that leaves the simulation domain is considered to be "open". We believe that the interaction of the CME flux with the open flux of the Sun can be better studied through idealized simulations, in which the isolation of such reconnection events can be better resolved, rather than in this complicated, realistic simulation. In addition, we favor the first explanation over the second because reconnection in the solar wind does not act to balance the flux increase owing to the introduction of the CME loops [e.g., *Owens and Crooker*, 2006], nor does it transport open flux on the Sun in the course of the solar cycle [e.g., *Owens et al.*, 2007]. At this stage, however, we leave the issue as an open question.

5. Summary and Conclusions

[34] Using numerical simulation, we study the evolution of a CME and its interaction with the coronal magnetic field based on the 12 May 1997, CME event. Our simulation provides the following results:

[35] • The simulated density corresponding to a cut across the CME at $1.1R_{\odot}$ is comparable to the coronal wave bright front that appears in the observed EIT images. This is similar to results obtained for another event studied by *Cohen et al.* [2009].

[36] • During the initial stage of CME expansion, the core flux rope reconnects with the surrounding (neighboring) field, which facilitates lateral expansion of the CME footprint in the low corona. Evidence for this is the displacement of the initial CME footpoints away from the source AR, via "stepping reconnection".

[37] • The CME then reconnects with the oppositely orientated overlying magnetic field in the manner of the breakout model. This is due to the global field topology, which is essentially the same as the initial state of the breakout model.

[38] • A significant component of the CME that expands into interplanetary space comprises one of the side lobes created mainly as a result of reconnection with the overlying field.

[39] • As the flux rope expands, it rotates counterclockwise by 90 degrees owing not to the kink instability but to reconnection with the surrounding fields.

[40] • The lateral expansion as well as the rotation of the flux rope due to interaction with the overlying magnetic field continue as long as the reconnections occur. They stop when the CME reaches the helmet streamers and the open flux, where the field of the CME matches the globally-organized field.

[41] • The orientation and left-handed chirality of the simulated flux rope are in agreement with the interplanetary flux rope observed at 1 AU.

[42] • The simulation shows no direct evidence of the anticipated interchange reconnection that would account for the electron observations indicating open fields in the CME at 1 AU.

[43] From these results we conclude that reconnection between closed loops may play a major role in transforming a small-scale flux rope in an active region to a large-scale flux rope with widely-spaced footpoints and a new orientation before leaving the Sun as a CME. Therefore, this complex interaction should be taken into consideration in any attempt to predict the CME geo-effectiveness. We further conclude that simulations of CMEs that erupt into realistic background fields constructed from magnetograms afford unprecedented views of the complicated three-dimensional development of magnetic structure.

[44] **Acknowledgments.** We thank for two referees for their useful comments and suggestions. O.C. and N.U.C. are supported by SHINE through NSF grants ATM-0823592 and ATM-0553397. N.A.S. was supported through the NASA LWS EMMREM project, grant NNX07AC14G. G.D.R.A. is supported by NASA grant NNX09AB11G-R. Simulation results were obtained using the Space Weather Modelling Framework, developed by the Center for Space Environment Modelling, at the University of Michigan with funding support from NASA ESS, NASA ESTO-CT, NSF KDI, and DoD MURI. SOHO is a project of international cooperation between ESA and NASA.

[45] Philippa Browning thanks the reviewers for their assistance in evaluating this paper.

References

Altschuler, M. D., and G. Newkirk (1969), Magnetic fields and the structure of the solar corona. I: Methods of calculating coronal fields, *Sol. Phys.*, *9*, 131–149, doi:10.1007/BF00145734.

Amari, T., J. F. Luciani, Z. Mikic, and J. Linker (2000), A twisted flux rope model for coronal mass ejections and two-ribbon flares, *Astrophys. J.*, *529*, L49–L52, doi:10.1086/312444.

Antiochos, S. K., C. R. DeVore, and J. A. Klimchuk (1999), A model for solar coronal mass ejections, *Astrophys. J.*, *510*, 485–493, doi:10.1086/306563.

Arge, C. N., and V. J. Pizzo (2000), Improvement in the prediction of solar wind conditions using near-real time solar magnetic field updates, *J. Geophys. Res.*, *105*, 10,465–10,479, doi:10.1029/1999JA900262.

Attrill, G., M. S. Nakwacki, L. K. Harra, L. van Driel-Gesztelyi, C. H. Mandrini, S. Dasso, and J. Wang (2006), Using the evolution of coronal dimming regions to probe the global magnetic field topology, *Sol. Phys.*, *238*, 117–139, doi:10.1007/s11207-006-0167-5.

Attrill, G. D. R., L. K. Harra, L. van Driel-Gesztelyi, and P. Démoulin (2007), Coronal "wave": Magnetic footprint of a coronal mass ejection?, *Astrophys. J.*, *656*, L101–L104, doi:10.1086/512854.

Attrill, G. D. R., L. van Driel-Gesztelyi, P. Démoulin, A. N. Zhukov, K. Steed, L. K. Harra, C. H. Mandrini, and J. Linker (2008), The recovery of CME-related dimmings and the ICME's enduring magnetic connection to the sun, *Sol. Phys.*, *252*, 349–372, doi:10.1007/s11207-008-9255-z.

Attrill, G. D. R., A. J. Engell, M. J. Wills-Davey, P. Grigis, and P. Testa (2009), Hinode/XRT and STEREO observations of a diffuse coronal "wave"-coronal mass ejection-dimming event, *Astrophys. J.*, *704*, 1296–1308, doi:10.1088/0004-637X/704/2/1296.

Biesecker, D. A., D. C. Myers, B. J. Thompson, D. M. Hammer, and A. Vourlidas (2002), Solar phenomena associated with "EIT waves", *Astrophys. J.*, *569*, 1009–1015, doi:10.1086/339402.

Boyd, T. J. M., and J. J. Sanderson (2003), *The Physics of Plasmas*, Cambridge Univ. Press, New York.

Burlaga, L., E. Sittler, F. Mariani, and R. Schwenn (1981), Magnetic Loop Behind an Interplanetary Shock: Voyager, Helios, and IMP 8 Observations, *J. Geophys. Res.*, *86*, 6673–6684.

Cohen, O., et al. (2007), A semi-empirical magnetohydrodynamical model of the solar wind, *Astrophys. J.*, *645*, L163–L166.

Cohen, O., I. V. Sokolo, I. I. Roussev, N. Lugaz, W. B. Manchester, T. I. Gombosi, and C. N. Arge (2008a), Validation of a global 3D heliospheric model with observations for the May 12, 1997 CME event, *J. Atmos. Sol. Terr. Phys.*, *70*, 583–592, doi:10.1016/j.jastp.2007.08.065.

Cohen, O., I. V. Sokolov, I. I. Roussev, and T. I. Gombosi (2008b), Validation of a synoptic solar wind model, *J. Geophys. Res.*, *113*, A03104, doi:10.1029/2007JA012797.

Cohen, O., G. D. R. Attrill, W. B. Manchester, and M. J. Wills-Davey (2009), Numerical simulation of an EUV coronal wave based on the 2009 February 13 CME event observed by STEREO, *Astrophys. J.*, *705*, 587–602, doi:10.1088/0004-637X/705/1/587.

Crooker, N. U., and D. F. Webb (2006), Remote sensing of the solar site of interchange reconnection associated with the May 1997 magnetic cloud, *J. Geophys. Res.*, *111*, A08108, doi:10.1029/2006JA011649.

Crooker, N. U., J. T. Gosling, and S. W. Kahler (2002), Reducing heliospheric magnetic flux from coronal mass ejections without disconnection, *J. Geophys. Res.*, *107*(A2), 1028, doi:10.1029/2001JA000236.

Crooker, N. U., S. W. Kahler, J. T. Gosling, and R. P. Lepping (2008), Evidence in magnetic clouds for systematic open flux transport on the Sun, *J. Geophys. Res.*, *113*, A12107, doi:10.1029/2008JA013628.

Delannée, C. (2009), The role of small versus large scale magnetic topologies in global waves, *Astron. Astrophys.*, *495*, 571–575, doi:10.1051/0004-6361:200809451.

Dere, K. P., et al. (1997), EIT and LASCO observations of the initiation of a coronal mass ejection, *Sol. Phys.*, *175*, 601–612, doi:10.1023/A:1004907307376.

Downs, C., I. I. Roussev, B. van der Holst, N. Lugaz, I. V. Sokolov, and T. I. Gombosi (2010), Toward a realistic thermodynamic magnetohydrodynamic model of the global solar corona, *Astrophys. J.*, *712*, 1219–1231, doi:10.1088/0004-637X/712/2/1219.

Fan, Y., and S. E. Gibson (2007), Onset of coronal mass ejections due to loss of confinement of coronal flux ropes, *Astrophys. J.*, *668*, 1232–1245, doi:10.1086/521335.

Forbes, T. G., and E. R. Priest (1995), Photospheric magnetic field evolution and eruptive flares, *Astrophys. J.*, *446*, 377, doi:10.1086/175797.

Forbes, T. G., et al. (2006), CME theory and models, *Space Sci. Rev.*, *123*, 251–302, doi:10.1007/s11214-006-9019-8.

Green, L. M., B. Kliem, T. Török, L. van Driel-Gesztelyi, and G. D. R. Attrill (2007), Transient coronal sigmoids and rotating erupting flux ropes, *Sol. Phys.*, *246*, 365–391, doi:10.1007/s11207-007-9061-z.

Kliem, B., V. S. Titov, and T. Török (2004), Formation of current sheets and sigmoidal structure by the kink instability of a magnetic loop, *Astron. Astrophys.*, *413*, L23–L26, doi:10.1051/0004-6361:20031690.

Landi, E., U. Feldman, and K. P. Dere (2002), CHIANTI-an atomic database for emission lines. V. Comparison with an isothermal spectrum observed with SUMER, *Astrophys. J.*, *139*, 281–296, doi:10.1086/337949.

Linker, J. A., Z. Mikić, R. Lionello, P. Riley, T. Amari, and D. Odstrcil (2003), Flux cancellation and coronal mass ejections, *Phys. Plasmas*, *10*, 1971–1978, doi:10.1063/1.1563668.

Lugaz, N., W. B. Manchester IV, I. I. Roussev, G. Tóth, and T. I. Gombosi (2007), Numerical investigation of the homologous coronal mass ejection events from active region 9236, *Astrophys. J.*, *659*, 788–800, doi:10.1086/512005.

Lynch, B. J., J. R. Gruesbeck, T. H. Zurbuchen, and S. K. Antiochos (2005), Solar cycle-dependent helicity transport by magnetic clouds, *J. Geophys. Res.*, *110*, A08107, doi:10.1029/2005JA011137.

Lynch, B. J., S. K. Antiochos, C. R. DeVore, J. G. Luhmann, and T. H. Zurbuchen (2008), Topological evolution of a fast magnetic breakout CME in three dimensions, *Astrophys. J.*, *683*, 1192–1206, doi:10.1086/589738.

Lynch, B. J., S. K. Antiochos, Y. Li, J. G. Luhmann, and C. R. DeVore (2009), Rotation of coronal mass ejections during eruption, *Astrophys. J.*, *697*, 1918–1927, doi:10.1088/0004-637X/697/2/1918.

Manchester, W. B., T. I. Gombosi, I. Roussev, A. Ridley, D. L. De Zeeuw, I. V. Sokolov, K. G. Powell, and G. Tóth (2004), Modeling a space weather event from the Sun to the Earth: CME generation and interplanetary propagation, *J. Geophys. Res.*, *109*, A02107, doi:10.1029/2003JA010150.

Manchester, W. B., IV, A. Vourlidas, G. Tóth, N. Lugaz, I. I. Roussev, I. V. Sokolov, T. I. Gombosi, D. L. De Zeeuw, and M. Opher (2008), Three-dimensional MHD Simulation of the 2003 October 28 coronal mass ejection: Comparison with LASCO coronagraph observations, *Astrophys. J.*, *684*, 1448–1460, doi:10.1086/590231.

Manoharan, P. K., L. van Driel-Gesztelyi, M. Pick, and P. Demoulin (1996), Evidence for large-scale solar magnetic reconnection from radio and X-ray measurements, *Astrophys. J.*, *468*, L73–L76, doi:10.1086/310221.

Moses, D., et al. (1997), EIT observations of the extreme ultraviolet sun, *Sol. Phys.*, *175*, 571–599, doi:10.1023/A:1004902913117.

Odstrcil, D., P. Riley, and X. P. Zhao (2004), Numerical simulation of the 12 May 1997 interplanetary CME event, *J. Geophys. Res.*, *109*, A02116, doi:10.1029/2003JA010135.

Odstrcil, D., V. J. Pizzo, and C. N. Arge (2005), Propagation of the 12 May 1997 interplanetary coronal mass ejection in evolving solar wind structures, *J. Geophys. Res.*, *110*, A02106, doi:10.1029/2004JA010745.

Ofman, L. (2007), Three-dimensional MHD model of wave activity in a coronal active region, *Astrophys. J.*, *655*, 1134–1141, doi:10.1086/510012.

Ofman, L., and B. J. Thompson (2002), Interaction of EIT waves with coronal active regions, *Astrophys. J.*, *574*, 440–452, doi:10.1086/340924.

Owens, M. J., and N. U. Crooker (2006), Coronal mass ejections and magnetic flux buildup in the heliosphere, *J. Geophys. Res.*, *111*, A10104, doi:10.1029/2006JA011641.

Owens, M. J., N. A. Schwadron, N. U. Crooker, W. J. Hughes, and H. E. Spence (2007), Role of coronal mass ejections in the heliospheric Hale cycle, *Geophys. Res. Lett.*, *34*, L06104, doi:10.1029/2006GL028795.

Pick, M., et al. (1998), Joint nancay radioheliograph and LASCO observations of coronal mass ejections - II. The 9 July 1996 event, *Sol. Phys.*, *181*, 455–468.

Podladchikova, O., and D. Berghmans (2005), Automated detection of eit waves and dimmings, *Sol. Phys.*, *228*, 265–284, doi:10.1007/s11207-005-5373-z.

Pohjolainen, S., et al. (2001), On-the-disk development of the halo coronal mass ejection on 1998 May 2, *Astrophys. J.*, *556*, 421–431, doi:10.1086/321577.

Powell, K. G., P. L. Roe, T. J. Linde, T. I. Gombosi, and D. L. de Zeeuw (1999), A solution-adaptive upwind scheme for ideal magnetohydrodynamics, *J. Comput. Phys.*, *154*, 284–309, doi:10.1006/jcph.1999.6299.

Riley, P., J. T. Gosling, and N. U. Crooker (2004), Ulysses observations of the magnetic connectivity between coronal mass ejections and the sun, *Astrophys. J.*, *608*, 1100–1105, doi:10.1086/420811.

Riley, P., R. Lionello, Z. Mikić, and J. Linker (2008), Using global simulations to relate the three-part structure of coronal mass ejections to in situ signatures, *Astrophys. J.*, *672*, 1221–1227, doi:10.1086/523893.

Roussev, I. I., T. G. Forbes, T. I. Gombosi, I. V. Sokolov, D. L. DeZeeuw, and J. Birn (2003a), A three-dimensional flux rope model for coronal mass ejections based on a loss of equilibrium, *Astrophys. J.*, *588*, L45–L48.

Roussev, I. I., T. I. Gombosi, I. V. Sokolov, M. Velli, W. Manchester, D. L. DeZeeuw, P. Liewer, G. Tóth, and J. Luhmann (2003b), A three-dimensional model of the solar wind incorporating solar magnetogram observations, *Astrophys. J.*, *595*, L57–L61.

Schmidt, J. M., and L. Ofman (2010), Global simulation of an extreme ultraviolet imaging telescope wave, *Astrophys. J.*, *713*, 1008–1015, doi:10.1088/0004-637X/713/2/1008.

Shen, F., X. Feng, S. T. Wu, and C. Xiang (2007), Three-dimensional MHD simulation of CMEs in three-dimensional background solar wind with the self-consistent structure on the source surface as input: Numerical simulation of the January 1997 Sun-Earth connection event, *J. Geophys. Res.*, *112*, A06109, doi:10.1029/2006JA012164.

Sokolov, I. V., K. G. Powell, O. Cohen, and T. I. Gombosi (2008), Computational magnetohydrodynamics, based on solution of the well-posed riemann problem, in *Numerical Modeling of Space Plasma Flows*, *Astron.*

Soc. Pacific Conf. Ser., vol. 385, edited by N. V. Pogorelov, E. Audit, and G. P. Zank, pp. 291–296, Astron. Soc. of Pacific, San Fransisco, Calif.

Thompson, B. J., S. P. Plunkett, J. B. Gurman, J. S. Newmark, O. C. St. Cyr, and D. J. Michels (1998), SOHO/EIT observations of an Earth-directed coronal mass ejection on May 12, 1997, *Geophys. Res. Lett.*, *25*, 2465–2468, doi:10.1029/98GL50429.

Titov, V. S., and P. Démoulin (1999), Basic topology of twisted magnetic configurations in solar flares, *Astron. Astrophys.*, *351*, 707–720.

Tóth, G., et al. (2005), Space weather modeling framework: A new tool for the space science community, *J. Geophys. Res.*, *110*, A12226, doi:10.1029/2005JA011126.

van der Holst, B., W. Manchester, I. V. Sokolov, G. Tóth, T. I. Gombosi, D. DeZeeuw, and O. Cohen (2009), Breakout coronal mass ejection or streamer blowout: The bugle effect, *Astrophys. J.*, *693*, 1178–1187, doi:10.1088/0004-637X/693/2/1178.

van Driel-Gesztelyi, L., C. P. Goff, P. Démoulin, J. L. Culhane, S. A. Matthews, L. K. Harra, C. H. Mandrini, K. Klein, and H. Kurokawa (2008), Multi-scale reconnections in a complex CME, *Adv. Space Res.*, *42*, 858–865, doi:10.1016/j.asr.2007.04.065.

Wang, Y.-M., and N. R. Sheeley (1990), Solar wind speed and coronal flux-tube expansion, *Astrophys. J.*, *355*, 726–732.

Webb, D. F., R. P. Lepping, L. F. Burlaga, C. E. DeForest, D. E. Larson, S. F. Martin, S. P. Plunkett, and D. M. Rust (2000), The origin and development of the May 1997 magnetic cloud, *J. Geophys. Res.*, *105*, 27,251–27,260, doi:10.1029/2000JA000021.

Wu, C., C. D. Fry, S. T. Wu, M. Dryer, and K. Liou (2007), Three-dimensional global simulation of interplanetary coronal mass ejection propagation from the Sun to the heliosphere: Solar event of 12 May 1997, *J. Geophys. Res.*, *112*, A09104, doi:10.1029/2006JA012211.

G. D. R. Attrill and O. Cohen, Harvard-Smithsonian Center for Astrophysics, 60 Garden St., Cambridge, MA 02138, USA. (ocohen@cfa.harvard.edu)

N. U. Crooker and N. A. Schwadron, Center for Space Physics, Boston University, 725 Commonwealth Ave., Boston, MA 02215, USA.

C. Downs, Institute for Astronomy, University of Hawaii at Manoa, 2680 Woodlawn Dr., Honolulu, HI 96822, USA.

T. I. Gombosi, Center for Space Environment Modeling, University of Michigan, 2455 Hayward, Ann Arbor, MI, 48109, USA.

M. J. Owens, Space Environment Physics Group, Department of Meteorology, University of Reading, Reading RG6 6BB, UK.